energies

MDPI

Article

Optimization of Performance and Efficiency of a Fuel-Flexible Free-Piston Linear Generator (FPLG) Engine for Range Extender Application

Alex Scopelliti, Daniela A. Misul, Fabrizio Santonocito and Mirko Baratta *

Energy Department, Politecnico di Torino, 10129 Torino, Italy; alex.scopelliti@polito.it (A.S.); daniela.misul@polito.it (D.A.M.); fabrizio.santonocito@polito.it (F.S.)
* Correspondence: mirko.baratta@polito.it; Tel.: +39-011-0904484

Abstract

In today's energy landscape, defined by the growing demand for sustainable energy generation technologies and the parallel need to advance internal combustion engine (ICE) architectures toward cleaner and more efficient solutions, the adoption of Free-Piston Linear Generator (FPLG) engines emerges as a highly promising approach. This innovative system enables the direct conversion of combustion-induced piston motion into electrical energy, eliminating the need for traditional crankshaft and connecting rod mechanisms. The FPLG concept facilitates efficient utilization of a broad spectrum of fuels—including methane, ethanol, LPG, gasoline, biodiesel, and hydrogen—by supporting variable compression ratio operation. This feature enhances operational flexibility and fuel adaptability, positioning the technology as a viable candidate for future energy transition scenarios. The absence of rotating mechanical components significantly reduces frictional losses, contributing to an overall increase in system efficiency. To accurately characterize and optimize engine performance, an extensive series of one-dimensional (1D) numerical simulations was performed under both free and controlled operating conditions. The resulting data enabled the development of semi-empirical models capable of predicting the dynamic behavior of the engine across a wide range of working scenarios. Finally, through a detailed parametric analysis, the optimal operating conditions were identified to maximize both net electric efficiency and electrical power output. These findings provide a solid ground for the design and implementation of FPLG engine systems in advanced power generation applications.

Keywords: IC engines; decarbonization; sustainability; fuel-flexible; control; engine modeling

check for updates

Academic Editor: Jiaqiang E

Received: 15 March 2026
Revised: 11 April 2026
Accepted: 20 April 2026
Published: 24 April 2026

Copyright: © 2026 by the authors. Licensee MDPI, Basel, Switzerland. This article is an open access article distributed under the terms and conditions of the Creative Commons Attribution (CC BY) license.

1. Introduction

The internal combustion engine remains the dominant propulsion technology for transportation, off-road machinery, and distributed power generation, mainly due to its robustness, maturity, and high energy density. However, increasing concerns related to climate change, air pollution, and fossil fuel depletion, together with progressively stricter CO_2 emission regulations, are driving a fundamental rethinking of conventional engine concepts. In particular, recent European Union legislation mandates near-zero CO_2 emissions for new passenger cars and light commercial vehicles from 2035 onward, effectively prohibiting the use of ICEs fueled by conventional fossil fuels. As a result, the role of the ICE must evolve to support the global energy transition, especially in sectors where full electrification remains impractical.

Despite significant advances in conventional engine technologies, further improvements in efficiency and emission reduction through incremental developments are becoming increasingly limited. Consequently, research efforts are shifting toward alternative fuels, advanced combustion concepts, and innovative powertrain architectures that can extend the relevance of ICEs in a low-carbon energy system. Future engine technologies must achieve high efficiency, fuel flexibility, low emissions, and effective integration with electrified power systems, while maintaining competitive power density and reliability.

In recent decades, the use of natural gas as a fuel for internal combustion engines has represented an important step toward decarbonization. The current state of the art in dedicated mono-fuel natural gas engines provides a solid technological basis for further research on hydrogen applications [1]. As a carbon-free fuel, H_2 is widely considered one of the main pathways for supporting the transition toward a sustainable energy system [2]. Hydrogen has emerged as a particularly promising alternative fuel for internal combustion engines due to its carbon-free combustion, wide flammability limits, high flame speed, and availability from renewable sources [3]. Hydrogen combustion can significantly reduce greenhouse gas emissions and virtually eliminate carbon-based pollutants, thus offering a viable pathway toward low-carbon propulsion while leveraging existing ICE infrastructure.

Due to political and economic drivers, biofuels, particularly ethanol, continue to increase their share in the automotive fuel market. A faster expansion of bioethanol engine technologies, along with a corresponding increase in market penetration, is expected with the development and commercialization of second-generation bioethanol processes. Long-term projections by the U.S. Energy Information Administration indicate that E85 could account for approximately 37% of domestic ethanol consumption in the United States by 2035.

The use of ethanol and ethanol–gasoline blends as transportation fuels shows significant potential. Several emissions are reduced when ethanol-containing fuels are used, with well-documented decreases in hydrocarbons (HC), carbon monoxide (CO), total hydrocarbons (THC), and non-methane hydrocarbons (NMHC). While some pollutants, particularly nitrogen oxides (NO_x), may remain unchanged or even increase, these effects can be mitigated through advanced engine technologies and optimized calibration strategies that exploit the specific properties of ethanol.

Recent modeling studies [4] suggest that ethanol could provide significant greenhouse gas (GHG) reduction potential in Europe, provided that engine hardware is designed to fully exploit its advantages, particularly its high octane number. Nevertheless, the large-scale deployment of high-ethanol-content fuels still requires further investigation, and several key research areas must be addressed to support both technological development and informed policy decisions.

A comparison between iso-octane and the tested fuels (NG, H_2, and ethanol) is reported in Table 1.

In the context of carbon peaking and carbon neutrality targets, the continued advancement of internal combustion engine technologies, particularly those utilizing clean fuels, remains a key research pathway toward sustainable, high-efficiency, and low-emission energy conversion systems. While alternative fuels such as NG, hydrogen, and ethanol offer significant decarbonization potential, their effective utilization requires engine architectures capable of accommodating wide variations in combustion characteristics and enabling flexible and efficient operation.

However, conventional ICE architectures, dominated by complex and heavy crank–link mechanisms, inherently limit further improvements in power density, combustion flexibility, and overall energy conversion efficiency. In particular, the geometrically fixed compression ratio of conventional engines restricts their ability to optimally adapt to fuels

with markedly different auto-ignition tendencies, flame speeds, and knock resistance. These limitations can be mitigated through alternative engine configurations, such as free-piston linear generators. By directly converting piston motion into electrical energy, FPLGs eliminate the crankshaft mechanism and enable flexible operation under both conventional and advanced combustion modes.

Table 1. Comparison of fuel properties.

Property	Iso-Octane [3]	Natural Gas (CH_4) [3,5]	Hydrogen [3]	Ethanol (E100) [4]
Molecular weight (g/mol)	114.236	16.04	2.016	46.07
Normal density (kg/m^3)	692	0.75–0.8	0.08	785–810
Boiling point (°C)	99	−161.5	−253	78.4
Mass diffusivity in air (cm^2/s)	∼0.07	0.16	0.61	–
Minimum ignition energy (mJ)	0.28	0.28	0.02	–
Minimum quenching distance (mm)	3.5	2.03	0.64	–
Burning limits (vol%)	1.1–6	5–15	4–75	3.3–19
Lower heating value (MJ/kg)	44.3	49.81	120	26.8
Higher heating value (MJ/kg)	47.8	55.5	142	∼29.7
Stoichiometric AFR (kg/kg)	15.0	17.2	34.2	8.97
Octane number (RON)	100	∼130	>130	108–110
Auto-ignition temperature (°C)	415	537	585	425

In recent years, several comprehensive literature reviews on free-piston linear generators (FPLGs) have been published [6–11]. In summary, an FPLG integrates a free-piston engine, a linear generator, and a rebound device into a single system. Its operating principle can be described as follows: high-temperature and high-pressure gases are generated within the combustion chamber of the free-piston engine, driving the piston assembly, which is directly coupled to the magnetic rod of the linear generator. The linear generator subsequently converts part of the linear kinetic energy of the magnetic rod into electrical energy. Compared with conventional reciprocating engines, FPLGs offer several advantages, including a shorter energy transmission chain and higher power density [12].

According to [9], these advantages primarily stem from the elimination of the crank–connecting rod mechanism, which reduces mechanical friction losses, shortens the energy conversion chain, and simplifies the mechanical structure. The free-piston configuration also enables variable compression ratio operation, thereby facilitating multi-fuel capability, as the engine compression ratio can be adjusted according to the fuel requirements and the target combustion mode (CI, SI, or advanced concepts such as Homogeneous Charge Compression Ignition (HCCI), as well as to the fuel octane or cetane number). Moreover, the faster expansion stroke and shorter high-temperature residence time near top dead center (TDC) contribute to higher thermal efficiency and reduced NO_x emissions. Owing to their compact structure and direct mechanical-to-electrical energy conversion, FPLGs are considered promising candidates for modular systems and hybrid-electric range extender applications.

Despite these advantages, FPLGs also present several significant challenges. The absence of a crankshaft mechanism results in unconstrained piston motion, leading to complex control requirements to maintain stable TDC and bottom dead center (BDC) positions, as well as a consistent compression ratio. Furthermore, the lack of flywheel energy storage makes engine starting and cold-start operation particularly challenging. Combustion stability remains a critical issue, since cycle-to-cycle variability can significantly influence piston trajectory and overall system performance. In dual-piston or opposed-

piston configurations, additional synchronization challenges arise, as imbalances between cylinders may lead to dynamic instability and degraded performance.

The main FPLG architectures are summarized in [9]. In particular, two-stroke FPLGs can be designed using port scavenging instead of valves, which simplifies the system and enables variable scavenging timing due to the absence of a crank mechanism and the resulting flexibility in the bottom dead center position. For all configurations, this flexibility allows adjustment of stroke length and compression ratio, thereby enabling adaptation of the power output. These additional degrees of freedom are expected to improve efficiency at both full load and, especially, part-load conditions, while also facilitating the effective utilization of a wide range of fuels.

Experimental research on FPLGs remains limited due to the significant challenges associated with control, particularly with regard to cycle-to-cycle variation, which requires robust control strategies to mitigate its effects [10]. Consequently, numerical studies play a crucial role in the development and optimization of this type of engine.

Among the available literature, Huang et al. [13] employed numerical CFD modeling to overcome the limited availability of prototypes, investigating hydrogen addition to methane in a glow-assisted ignition FPLG. This approach enabled detailed performance and emissions analyses, showing, for example, that the heat release rate (HRR) increases with hydrogen addition. High hydrogen concentrations can lead to overly advanced combustion, resulting in increased compression negative work. Furthermore, hydrogen addition substantially increases in-cylinder temperatures, leading to higher NO_x emissions while reducing CO formation. These insights provide valuable guidance for the design and planning of subsequent experimental campaigns.

Among the considered configurations, the opposed-piston layout stands out as particularly promising, especially when combined with advanced combustion strategies enabled by a variable compression ratio, offering significant potential for high thermal efficiency.

Schneider et al. [14] analyzed the implementation of HCCI combustion, enabled by the capability of the FPLG to vary scavenging timing and compression ratio. This advanced combustion mode increased the indicated efficiency from 37.6% to 46.9%, due to the very fast combustion achieved through mixture self-ignition and reduced wall heat transfer resulting from lower combustion temperatures, which together enhance piston work.

In their study, Zhang et al. [15] achieved an indicated thermal efficiency of 39.7% in a gasoline-fueled opposed-piston free-piston engine by optimizing the fuel spray angle. Building on this work, Liu et al. [16] highlighted the importance of optimizing the scavenging process. Using a single-channel approach, they reduced the combustion duration by 59.8%; however, this resulted in a lower indicated efficiency due to limitations in the fresh charge, yielding a value of 37.2%. In contrast, a dual-channel configuration achieved a higher indicated efficiency of 40.9%.

In addition, the opposed-piston configuration, with appropriate synchronization of the piston units, allows complete compensation of mass forces. Combined with a compact and flat design, the FPLG is well suited for use in hybrid vehicles [14].

The present paper focuses on the application of a 1D model, developed and validated in [17], for the performance and efficiency characterization of an opposed-piston FPLG unit under different compression ratios and fuel characteristics. The paper presents a systematic and comprehensive investigation of the fluid-dynamic and thermodynamic behavior and performance, which is currently lacking in the literature. In particular, the objective of the paper is to demonstrate that comparable levels of power and efficiency can be achieved with different fuels, highlighting the flexibility of FPLG operation. The study was carried out using the Gasdyn software. First, a Design of Experiments (DoE) methodology was applied to systematically investigate the behavior of the free-piston linear generator under

different operating conditions. This approach ensures uniform coverage of the design space while avoiding redundant parameter combinations. Subsequently, a correlation analysis was performed to quantify the magnitude and structure of the combined effects of the selected input parameters on engine performance. This analysis enables the identification of dominant trends, interdependencies, and potential synergistic or antagonistic interactions among the variables.

Based on these results, a performance and efficiency assessment was conducted for three different fuels (NG, H_2, and ethanol) while varying key parameters, particularly the compression ratio (CR).

2. Reference Engine and Model Description

The engine considered in the present work is an opposed-piston two-stroke engine with 'uniflow' scavenging, which has been proposed as a possible range-extender solution for passenger cars [17]. The main geometric characteristics of the engine are summarized in Table 2. The nominal engine displacement is 250 cm^3, including the volume swept by both cylinders. Consistently with the previous study, the system includes an electrically driven supercharger with an isentropic efficiency of 75%. The choice of constant efficiency was made to avoid introducing a dependency of the results on a specific turbocharger, thereby improving the generality of the analysis. In practice, the actual supercharger efficiency depends on the corrected mass flow rate and pressure ratio. It is worth mentioning that the variation in the compressor operating point is significantly lower than in turbine-driven compressors, due to the fixed compressor speed imposed by the electric motor. For this reason, the constant efficiency assumption does not prevent the model from capturing the main performance trends. Finally, it is worth pointing out that direct fuel injection is performed after exhaust port closure, so as to minimize fuel slip during the scavenging process.

Table 2. Main thermal engine geometry data.

Parameter	Value
Nominal total stroke	99 mm
Nominal total displacement	248 cm^3
Nominal compression ratio	12
Intake ports distance from TDC_{nom}	37.23 mm
Intake ports height	12.27 mm
Intake ports total width	109.92 mm
Exhaust ports distance from TDC_{nom}	35.15 mm
Exhaust ports height	14.35 mm
Exhaust ports total width	101.88 mm

Figure 1 reports a scheme of the numerical model applied in this paper for the investigation of the behavior of the free-piston engine. The model was developed and validated in [17]. It is based on the application of Newton's Law and requires the combination of several sub-models for the evaluation of the forces acting on the piston. More in detail:

- Thermo-fluid dynamic model of the IC engine, including the 1D simulation of the unsteady flow in intake and exhaust manifolds;
- Model for the evolution of the pressure inside the gas spring;
- Model for the description of the electric circuit of the linear generator and its interaction with the piston kinematics.

The 1D thermo-fluid-dynamic model was developed with the support of 3D CFD simulations. Although a complete description of the model development and validation is

available in [17], a few details are reported here. Since the 1D discretization cannot capture the complex wave patterns induced by ports and junctions, an iterative 1D–3D procedure was implemented until convergence was achieved. The 3D model was run using the piston position obtained from the 1D model as input, and the system discretization in the 1D model was modified to reproduce the wave patterns predicted by the 3D model. The latter was also used for the steady-state evaluation of the discharge coefficients of each port.

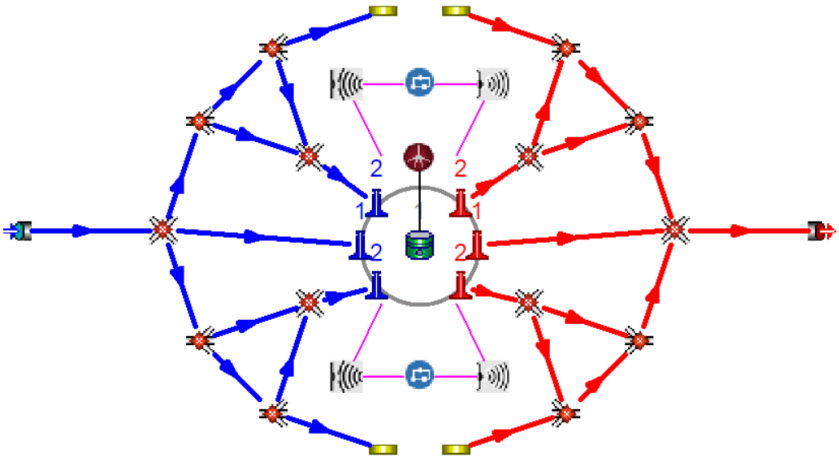

Figure 1. 1D model implemented in Gasdyn.

A non-predictive combustion model based on the Wiebe formulation was applied. The combustion duration and the Wiebe exponent for the NG case were defined based on the results of 3D reactive-flow simulations. It was verified that the shape factor and exponent of the Wiebe formulation have a negligible influence on the results. Regarding the combustion duration, a sensitivity analysis was carried out, with the following results:

The combustion duration (0–100%) was varied in the range of 1–5 ms, and a negligible effect on MFB50 was observed. This is due to the action of the PI controller on the ignition position, which in turn adjusts the TDC position, as discussed below. As shown in Table 3, the predicted indicated efficiency is almost independent of the combustion duration, whereas a ±67% variation in the latter results in a 10–15% change in the PFP. For this reason, the analyses presented in Section 5 were carried out by keeping the Wiebe parameters constant.

Table 3. Sensitivity analysis on combustion duration for $p_{\text{intake}} = 1.5$ bar and $GLC = 250$ Ns/m with NG fueling, $\lambda = 1$.

Combustion Duration [ms]	η_i [-]	Ignition Position [mm]	MFB50 [mm]	p_{max} [bar]
1	0.276	3.4	2.0	133.8
3	0.276	6.1	2.1	128.5
5	0.278	9.0	2.3	119.0

Regarding heat transfer, in the absence of significant soot production, radiative heat transfer can be neglected [18,19], allowing the Woschni coefficients to be kept constant across different fueling conditions. This assumption is justified by the observation that in-cylinder and combustion-induced fluid velocities are not significantly affected by the fuel type.

Given the absence of a traditional crank–slider mechanism, the piston displacement depends on the forces acting on it:

$$m_p \ddot{x}_p = F_p - F_{gs} - F_{el} - F_f \tag{1}$$

where m_p is the piston mass and $\ddot{x}_p$ is the piston acceleration. The forces acting on the piston include the pressure force generated within the cylinder (F_p), the friction force (F_f), the gas spring force (F_{gs}), and the electromagnetic force produced by the linear generator (F_{el}).

The gas-spring force is obtained by assuming that the corresponding chamber pressure follows the following polytropic-like relation:

$$pV^n = p_0 V_0^n \tag{2}$$

where n is a user-defined polytropic index, p_0 is the initial gas spring pressure specified at the beginning of the simulation, and V_0 is the corresponding initial volume.

Both the linear-generator force and the mechanical friction force are assumed to be proportional to the piston velocity, according to

$$F_f = -C_f v_p \tag{3}$$

$$F_{el} = -C_{el} v_p \tag{4}$$

where v_p is the instantaneous piston velocity, C_f is the friction coefficient and C_{el} is the generating load coefficient (GLC). This coefficient depends on the electrical characteristics of the generator and represents a key parameter governing the energy conversion process. Assuming a constant GLC implies that the electrical load is purely resistive and that the magnetic circuit operates in its linear region [20].

During the simulations, the engine compression ratio was controlled by means of two proportional–integral (PI) controllers:

- The first controller adjusted the ignition position (i.e., the piston position at which combustion is triggered) in order to achieve the target TDC position;
- The second controller adjusted the initial gas-spring pressure, p_0, based on the difference between the actual and the target BDC positions.

It is worth noting that two definitions of the compression ratio were adopted in this study.

- The volumetric (nominal) compression ratio is defined as the ratio of the maximum to the minimum chamber volume, i.e., the combustion chamber volume at BDC and TDC, respectively;
- The 'effective' compression ratio is defined as the ratio between the chamber volume at exhaust port closure and the minimum chamber volume.

The effective compression ratio is always lower than the nominal one and more accurately represents the actual compression stroke experienced by the air–fuel mixture. It is worth noting that the TDC controller alone would be sufficient to control the effective CR. However, control of the BDC position is required to avoid excessive piston stroke, which would lead to reduced scavenging efficiency, lower engine frequency, and, consequently, lower rated power.

3. System Characterization Through Design of Experiments

The first part of the study consisted of a characterization of the engine behavior by means of a Design of Experiments (DoE) analysis. This technique is widely used in problems involving a large number of state variables. Moreover, it allows cause–effect relationships between variables to be identified, thereby supporting the characterization of engine performance and its dependence on design and operating parameters. Once the lower and upper bounds of the input variables were defined and the total number of

simulations was selected, the DoE tool generated a set of statistically distributed sampling points within the prescribed domain. These points represent distinct operating conditions at which the numerical model was evaluated.

In this work, three independent input variables were considered:

- Intake pressure;
- Generating load coefficient;
- Effective compression ratio.

A 'full factorial' exploration of the parameter space would have required n^3 simulations, where n denotes the number of discrete values assumed by each variable within its respective range. Instead, the adopted DoE approach significantly reduced the computational cost while preserving the ability to capture both the individual and combined effects of the selected parameters. The operating ranges selected for each independent variable are summarized in Table 4.

Table 4. Operating parameter ranges considered in the analysis.

Parameter	Lower Limit	Upper Limit	Units
Intake Pressure	1.1	2	bar
Generating Load Coefficient	150	450	Ns/m
Effective Compression Ratio	8	12	–

The selected ranges of the input variables were considered appropriate for the objectives of the present study, as they allow exploration of a sufficiently wide range of feasible operating conditions. In particular, selecting a specific GLC value corresponds to assuming a given value of the equivalent resistive load, which is controlled by the generator power electronics in the real system.

The dataset obtained from the previously described simulation campaign was post-processed and analyzed through a correlation analysis in order to quantify the strength of the cause–effect relationships among the model output variables, as well as to identify possible synergistic or compensating interactions between them.

Based on the results of the correlation analysis, suitable regression models were developed to better understand the dependence of engine performance on the independent variables (input parameters). In particular, these models enable rapid preliminary screening of unfavorable parameter combinations, allowing certain design or operating choices to be discarded at an early stage of the development process. For this reason, the construction of surrogate models based on the available simulation data represents an effective strategy to reproduce the relationships between the independent variables and the performance outputs.

A fundamental prerequisite for a robust and reliable Design of Experiments is the careful selection of the input parameters and the appropriate definition of their variation ranges, in order to ensure adequate coverage of the design space. To this end, the Sobol sequence [21] was adopted to generate a set of quasi-random sampling points. The Sobol method, belonging to the class of low-discrepancy quasi-random generators, ensures a uniform and space-filling distribution of samples, which is particularly advantageous for high-dimensional problems. The Sobol sequence was selected due to its generally good performance compared to other sampling methods [22].

Out of the 200 simulations initially scheduled, 151 were successfully completed, corresponding to 75.5% of the total dataset. The remaining simulations resulted in numerical failures, likely associated with intrinsically critical operating conditions, as discussed in the following paragraph. A three-dimensional visualization of the tested points as a function of the three input parameters is shown in Figure 2a. The successful simulations are indicated

by empty circles in Figure 2, while red solid circles identify the simulations for which the model did not converge to a stable solution.

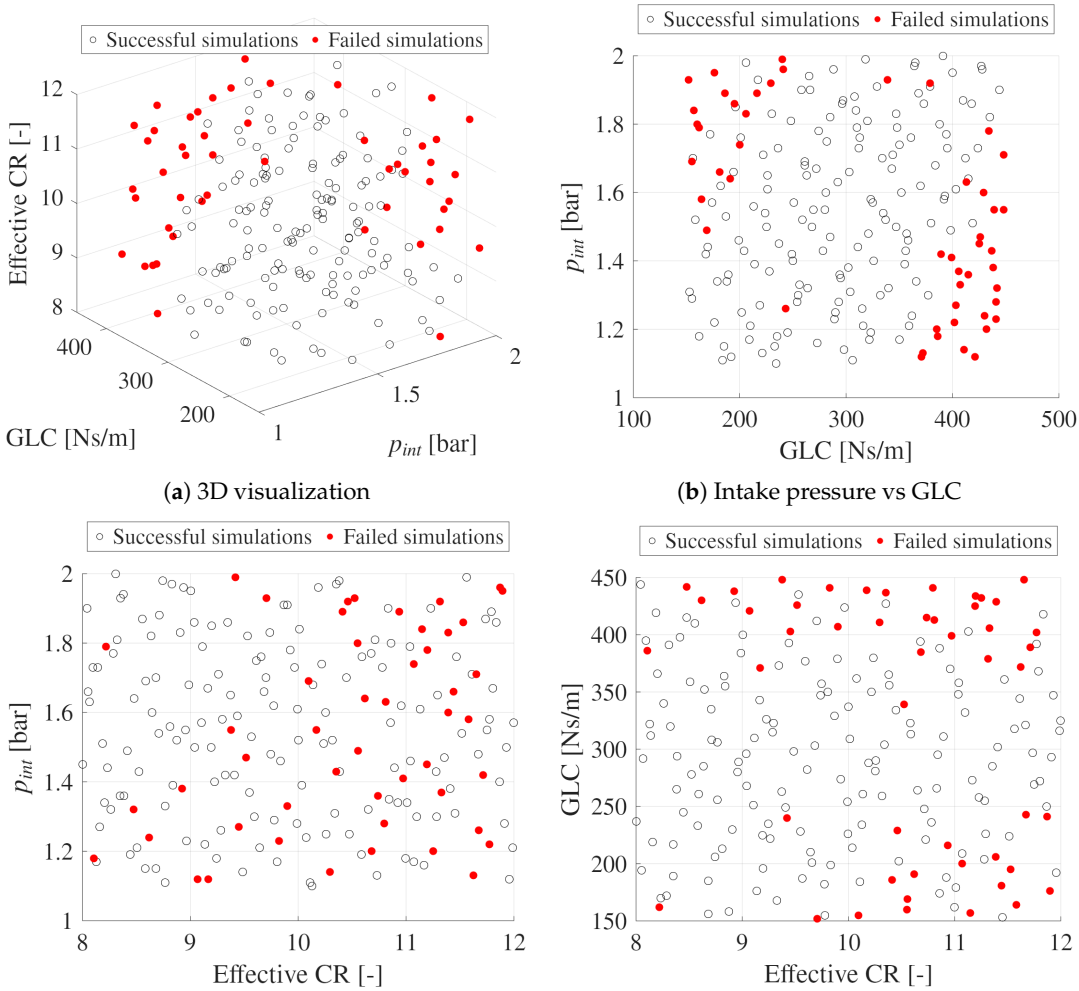

(**a**) 3D visualization (**b**) Intake pressure vs GLC

(**c**) Intake pressure vs Effective CR (**d**) GLC vs Effective CR

Figure 2. DoE distribution for the 200 simulations. (**a**) Three-dimensional visualization of the sampled design space as a function of intake pressure, GLC, and effective CR. (**b**–**d**) Two-dimensional projections of the sampled points highlighting the pairwise relationships between the input parameters: (**b**) intake pressure vs GLC, (**c**) intake pressure vs effective CR, and (**d**) GLC vs effective CR.

Figure 2b highlights two distinct regions of the design space in which the simulations systematically failed, specifically located at the top-left and bottom-right corners. In these regions, the simulations were unsuccessful either because the piston stopped before reaching port opening or due to excessively retarded combustion timing, which led to a non-physical negative chamber volume. Although this behavior originates from a numerical transient associated with the iterative solution procedure, it is indicative of potentially unstable engine operation, considering that the Gasdyn solver is a state-of-the-art tool specifically developed for stiff numerical problems involving gas-dynamic discontinuities [23,24].

Stable engine operation is observed for operating conditions distributed along the bisector of the first quadrant. From a physical perspective, this indicates that higher intake pressures should be selected as the generator load increases. Conversely, Figure 2c shows that unsuccessful operating points are scattered in the intake pressure vs effective CR plane, suggesting no clear influence of this parameter on system stability. Finally, Figure 2d highlights stable behavior in the mid-range of GLC values, while limitations arise near the

bounds, as already observed in Figure 2b. Similarly, no specific influence of the compression ratio could be identified, in agreement with Figure 2c.

4. Correlation Analysis

The data obtained from the Design of Experiments were processed by means of a correlation analysis in order to identify the main cause–effect relationships among the parameters. The analysis focuses exclusively on the three input variables defined in the Sobol sequence. Regarding the dependent output variables, the performance parameters listed in Table 5 were considered.

Table 5. Dependent output performance parameters.

Dependent Output Variable	Notation	Units
Indicated Mean Effective Pressure	IMEP	bar
Indicated Efficiency	η_i	—
Brake Specific Fuel Consumption	BSFC	g/kWh
Net Electric Power	$P_{el,net}$	kW
Maximum in-cylinder Pressure	p_{max}	bar

Based on these data, regression models were developed to estimate the effects of variations in the input parameters, as well as to support the definition of guidelines for engine and generator design. The linear correlation between two variables can be defined in several ways. One of the most commonly used methods is the Pearson correlation coefficient (PCC) [25], defined as the ratio between the covariance of the two variables and the product of their standard deviations. For each pair of variables (i, j), the PCC is computed as follows:

$$\rho(X_i, Y_j) = \frac{\mathrm{cov}(X_i, Y_j)}{\sigma_{X_i}\,\sigma_{Y_j}} \tag{5}$$

where:

- $\rho(X_i, Y_j)$ is the linear correlation coefficient between the variables X_i and Y_j;
- $\mathrm{cov}(X_i, Y_j)$ is the covariance between X_i and Y_j;
- σ_{X_i} and σ_{Y_j} are the standard deviations of X_i and Y_j, respectively.

The Pearson correlation coefficient $\rho(X_i, Y_j)$ is dimensionless and ranges between -1 and 1. Values between $+0.5$ and $+1$ indicate a strong positive correlation, with a value of $+1$ corresponding to a perfect direct relationship. Conversely, values between -0.5 and -1 indicate a strong negative correlation, with -1 corresponding to a perfect inverse relationship. A value of $\rho(X_i, Y_j) = 0$ indicates no linear correlation between the two variables.

The application of the correlation coefficient demonstrated that the input parameters are independent and not significantly correlated with each other. This is important to avoid redundancy in the effects of the input variables. Intake pressure and generating load coefficient show a PCC of 0.35, indicating a weak correlation. This result is physically consistent, as it reflects the higher energy demand associated with increasing load.

Figure 3 displays the Pearson correlation coefficient ρ for each input and output considered. Based on the definition of correlation, the higher the absolute value of ρ, the stronger the influence of a given input variable on the corresponding performance parameter. Moreover, the analysis allows the effect of each independent variable on a specific output to be identified. For example, the Generating Load Coefficient and the intake pressure have a direct influence on the engine IMEP, with correlation coefficients of 0.92 and 0.67, respectively. On the other hand, GLC has only a limited effect on the maximum in-cylinder pressure, p_{max}. This result is physically consistent when the action

of the PI controller on the TDC position is considered. In fact, a higher GLC leads to a reduction in ignition advance, thereby compensating for the increase in p_{max}.

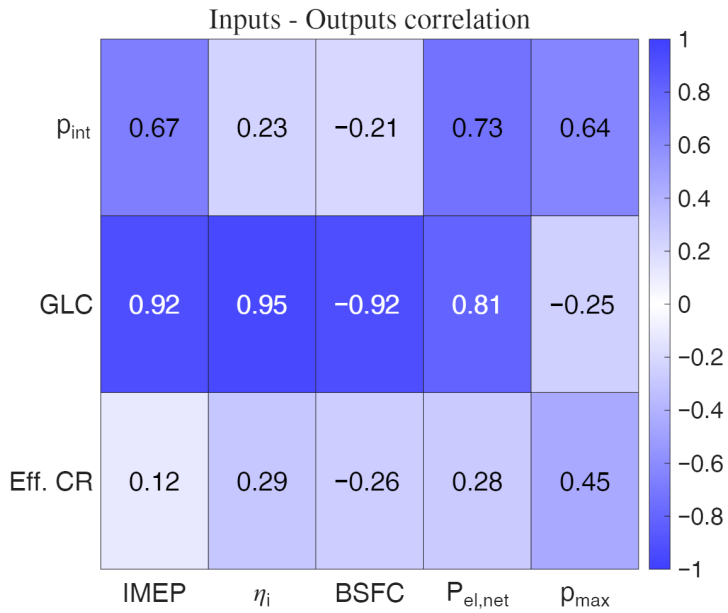

Figure 3. Inputs-Outputs correlation for $\rho > 0.2$.

Overall, the Generating Load Coefficient plays a significant role in many performance parameters, while the compression ratio has a secondary influence in most cases. However, it is important to consider the combined effect of the input variables on the outputs, rather than focusing solely on individual input–output relationships. In light of this, once the impact of each input variable on a given output parameter has been quantified through the PCC, this information can be used to construct regression models.

Two different analyses were carried out: the first considering only inputs with correlation coefficients greater than 0.4, and the second including inputs with coefficients greater than 0.2. Regression-based predictive models are widely used in the analysis and optimization of free-piston engine generators, particularly within response surface methodology frameworks, where quadratic models are often adopted to capture nonlinear interactions between operating and design parameters [26]. The mathematical models selected for this purpose are the following:

- Linear model:

$$y = c_0 + \sum_{k=1}^{n} c_k \cdot x_k \tag{6}$$

- Quadratic model:

$$y = c_0 + \sum_{k=1}^{n} c_k \cdot x_k + \sum_{k=1}^{n} c_{kk} \cdot x_k^2 + \sum_{k<l} c_{kl} \cdot x_k \cdot x_l \tag{7}$$

- Polynomial model:

$$y = \sum_{k=1}^{n} c_k \cdot x_k^{e_k} \tag{8}$$

- Power-law model:

$$y = C \cdot \prod_{k=1}^{n} x_k^{e_k}, \tag{9}$$

where y is the analyzed output, c_0 is the intercept term, x_k is the k-th input variable, and c_k is the coefficient associated with the k-th input variable. The parameter n denotes the number of input variables considered in the fitting procedure. The coefficient c_{kk} represents the quadratic coefficient associated with the k-th input variable, while c_{kl} is associated with the interaction term between the k-th and l-th input variables. The parameter e_k is the exponent associated with the k-th input variable, and C is the multiplicative constant. For each model, the corresponding coefficients were calibrated using the results of the DoE simulations.

To assess the robustness of the predictive models, the dataset obtained from the Gasdyn simulations was randomly divided into two subsets. The first subset, comprising 80% of the total data, was used as the training set to determine the model coefficients using MATLAB v.2025 routines. The remaining 20% was used to validate the regression models (validation dataset).

Two parameters were used to rank the performance of the models, namely, Coefficient of Determination (R^2) and Root Mean Square Error ($RMSE$). The R^2 coefficient is normally defined between 0 and 1, and gives a measure of how the original scatter is close is the regression curve. The $RMSE$ value is a measure of accuracy consisting in the quadratic mean of the differences between the actual data and the ones predicted by the model. Its value is always non-negative and an ideal value of $RMSE = 1$ corresponds to a perfect fit of the data. High R^2 and low $RMSE$ are an indication of high rank of the regression.

For each output, the independent variables were selected based on a ρ threshold, which was compared to the values in Figure 3. As stated above, two threshold correlation values were considered, in order to select the independent variables to be considered, 0.4 and 0.2. This was chosen so as to verify the effect of the threshold definition on the regression curve accuracy, although a correlation of 0.4 is generally considered to be low. For each of the performance parameters listed in Table 5, the results of both analyses are reported in Tables 6–9. The correlations showing the best results for the indicators have been highlighted in green.

Table 6. R^2 values for each mathematical model for $\rho > 0.4$.

Parameter	Linear	Quadratic	Polynomial	Power-Law
IMEP	0.971	0.982	0.967	0.978
η_i	0.907	0.926	0.917	0.917
BSFC	0.855	0.942	0.479	0.479
$P_{el,net}$	0.871	0.916	0.862	0.890
p_{max}	0.682	0.661	0.685	0.676

Table 7. R^2 values for each mathematical model for $\rho > 0.2$.

Parameter	Linear	Quadratic	Polynomial	Power-Law
IMEP	0.971	0.982	0.967	0.978
η_i	0.990	0.999	0.997	0.997
BSFC	0.928	0.997	0.957	0.523
$P_{el,net}$	0.972	0.998	0.957	0.985
p_{max}	0.934	0.991	0.946	0.923

Table 8. RMSE values for each mathematical model for $\rho > 0.4$.

Parameter	Linear	Quadratic	Polynomial	Power-Law	Units
IMEP	0.412	0.325	0.442	0.358	[bar]
η_i	0.017	0.015	0.016	0.016	[-]
BSFC	22.32	14.13	42.24	42.24	[g/kWh]
$P_{el,net}$	0.677	0.548	0.701	0.626	[kW]
p_{max}	11.79	12.17	11.73	11.89	[bar]

Table 9. RMSE values for each mathematical model for $\rho > 0.2$.

Parameter	Linear	Quadratic	Polynomial	Power-Law	Units
IMEP	0.412	0.325	0.442	0.358	[bar]
η_i	0.006	0.002	0.003	0.003	[-]
BSFC	15.66	3.156	12.12	40.43	[g/kWh]
$P_{el,net}$	0.316	0.091	0.390	0.228	[kW]
p_{max}	5.388	1.937	4.846	5.817	[bar]

The results in the tables show very high values for the coefficient of determination R^2, particularly for the Quadratic model. This is also due to the use of a deterministic 1D simulation environment to generate the dataset. Measurement errors and calculation chain uncertainty of experimental data would have decreased the R^2 value of each regression. Decreasing the threshold for ρ from 0.4 to 0.2 leads to markedly improved results. In particular, the coefficient of determination for the maximum in-cylinder pressure increases from 0.69 to 0.99, corresponding to an improvement of approximately 30% in prediction accuracy. Regarding the choice of the model, the results indicate that, in nearly all cases, the quadratic model provides the best results in terms of both $RMSE$ and R^2. This is observed for both values of ρ. As far as the RSME results are concerned (Tables 6 and 7), some of the parameters, such as, IMEP and η_i, do not change by reducing ρ, or change to a very minor extent. This is consistent with the correlation values reported in Figure 3. In fact, a reduction of ρ to 0.2 does not allow the third variable in Figure 3 to be included for the IMEP regression line definition. In the case of η_i and BSFC, the ρ reduction allows the effective compression ratio to be included, and the performance of the model are significantly improved, despite the rather poor correlation of the performance variables with CR.

Figure 4 further illustrates some of the results obtained using the various models for $\rho > 0.2$. Consistent with the aforementioned observations, the plots depict the training data points in blue and the validation points in red. The x-axis corresponds to the parameters obtained from numerical simulations, while the y-axis represents the results predicted by the correlation model. The central black line denotes perfect agreement between the actual results and the model predictions. The corresponding RMSE and R^2 values are also reported.

Overall, the models developed in this section are capable of describing the influence of the main design and operating parameters on the engine behavior with good accuracy. With reference to CNG fueling and stoichiometric operation, the main outcomes from this section are:

- the Generating Load Coefficient exerts a dominant influence on IMEP, indicated efficiency, BSFC, as well as Net electric power;

- the effective CR showed a minor effect on most parameters: this suggests that the CR can be chosen based on the risk of abnormal combustion, taking the fuel properties and the working conditions into account;
- for an optimization of the engine efficiency and specific power, the generating load should be selected at its maximum value, for a given intake pressure.

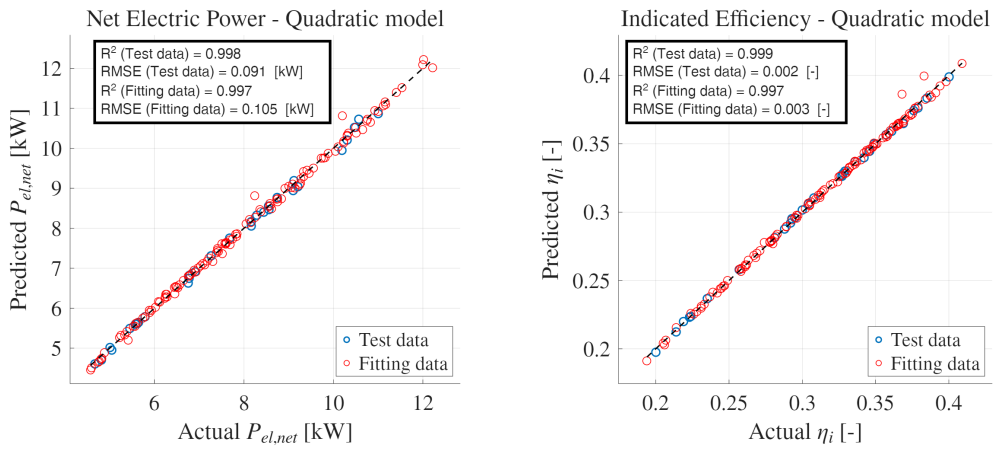

(**a**) Net electric power correlation (**b**) Indicated efficiency correlation

Figure 4. Comparison between numerical simulation results and correlation model predictions for $\rho > 0.2$: (**a**) net electric power and (**b**) indicated efficiency. Training data points are shown in blue, while validation points are shown in red. The black line represents perfect agreement between simulations and model predictions. The corresponding RMSE and R^2 values are also reported.

5. Engine Performance Optimization

Following the comprehensive characterization of the engine behavior discussed in the previous section, the modeling activity presented here aims to analyze engine performance and efficiency, with the objective of optimizing the trade-off between these two aspects. In addition, alternative fuels are considered in order to demonstrate the fuel-flexibility potential of the free-piston engine.

Initially, variations in the air–fuel equivalence ratio, generating load coefficient, and compression ratio are analyzed using hydrogen as the fuel. Subsequently, exploiting the capability of the free-piston engine to operate with a variable compression ratio, several fuels are compared, namely natural gas, hydrogen at $\lambda = 1$ and $\lambda = 2$, and ethanol.

5.1. Lambda and GLC Sweep Characterization in Hydrogen Combustion

Figure 5 illustrates the effects of the simultaneous variation in the air–fuel equivalence ratio and the generating load coefficient on the main power-related and efficiency indicators. The analysis is performed using hydrogen as fuel, at a fixed compression ratio of 13 and a constant pressure difference Δp between intake and exhaust manifolds. Two different intake pressure conditions are considered. In the plots, the dependent variables are reported as a function of GLC. Different line styles and symbols identify the λ values, while colors indicate the intake pressure. The minimum and maximum values associated with each curve represent the lower and upper limits of the load for a given combination of intake pressure and λ.

Figure 5a shows that the maximum achievable indicated efficiency increases with increasing λ. This behavior can be attributed to a more effective utilization of the available chemical energy, resulting from lower peak temperatures and reduced heat losses. The higher efficiency observed at higher loads is due to the fact that the indicated cycle approaches the reference Otto air–fuel cycle. This is consistent with the results reported in [17].

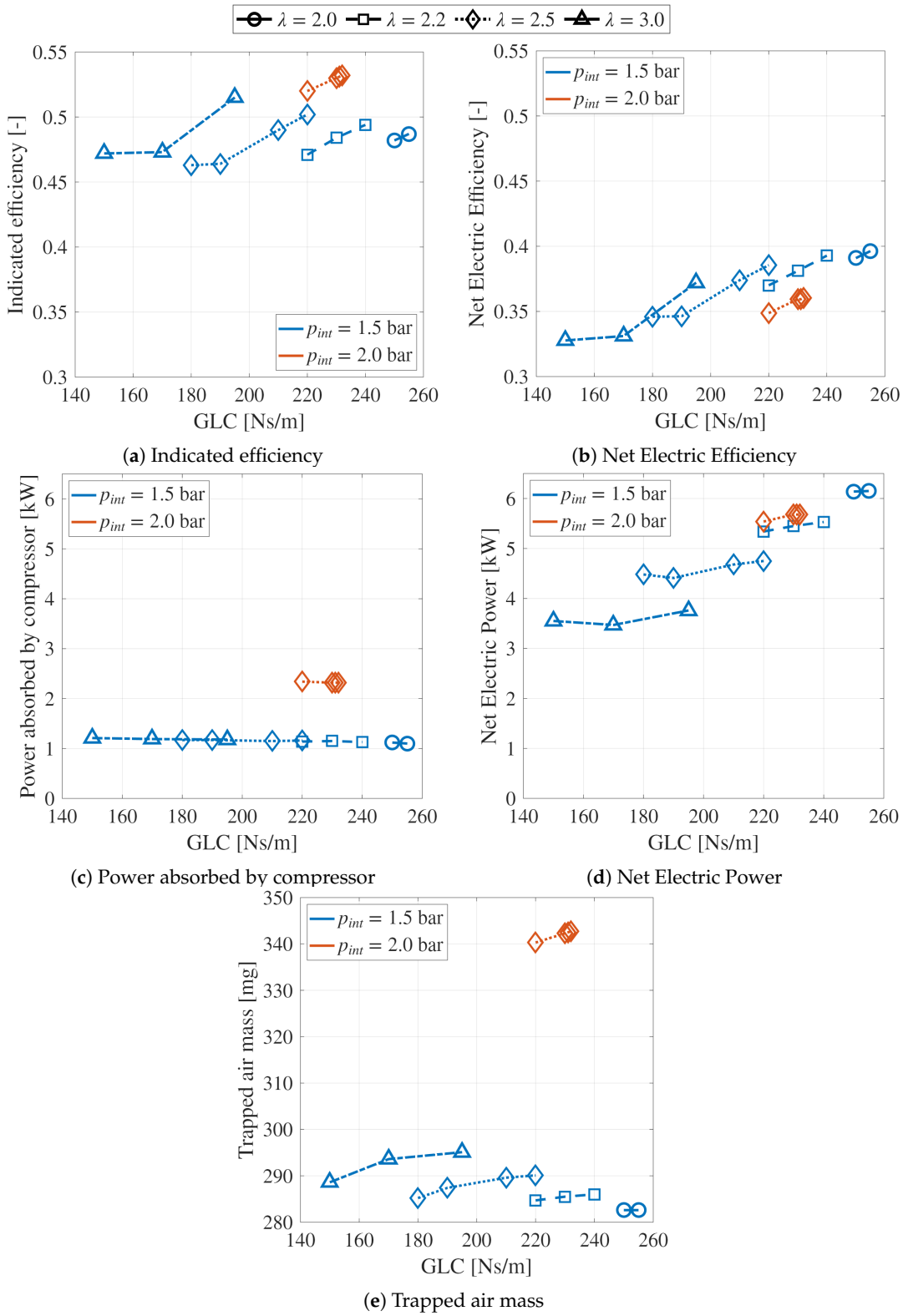

(**a**) Indicated efficiency (**b**) Net Electric Efficiency

(**c**) Power absorbed by compressor (**d**) Net Electric Power

(**e**) Trapped air mass

Figure 5. Effect of the simultaneous variation in the λ and GLC using hydrogen fuel. Results are shown for a compression ratio of 13 and constant pressure difference Δp under two intake pressure conditions: 1.5 bar (blue) and 2.0 bar (orange). The different λ values are indicated by the line and marker styles shown in the legend. Plots report: (**a**) indicated efficiency, (**b**) net electric efficiency, (**c**) compressor absorbed power, (**d**) net electric power, and (**e**) trapped air mass.

It is also observed that the achievable efficiency increases with increasing intake pressure, due to the reduced relative contribution of heat losses at higher loads. Moreover,

the maximum achievable load varies with the selected λ value. The trapped air mass mainly depends on the intake pressure p_{int} (see Figure 5e). An increase in λ corresponds to a decrease in the fuel mass injected into the cylinder and, consequently, to a lower fuel energy per cycle. The increased air mass flow also leads to higher compressor power demand (Figure 5c), which, at the same λ, becomes nearly twice as large as in the lower-pressure configuration. This also explains why the net electric efficiency (Figure 5b) shows trends with respect to λ and p_{int} that are opposite to those of the indicated efficiency (Figure 5a).

Using increasingly lean mixtures does not result in a significant variation in the compressor power. This is because the air-to-fuel ratio is controlled by the injected fuel mass; therefore, variations in the trapped air mass are mainly due to differences in piston motion and the resulting scavenging process. Figure 5d shows that leaner mixtures lead to a significant reduction in net power output. This effect is primarily related to the lower energy content of the mixture, as well as to the absence of a system for recovering exhaust energy, as already discussed in [17].

5.2. CR Effect on Engine Performance Under Hydrogen Fueling

The results discussed in the previous subsection further confirm the advantage of setting the maximum achievable GLC in order to maximize net power output and efficiency for each operating condition. The simulations presented in this subsection were carried out under these conditions, with the aim of investigating engine behavior under different compression ratios and intake pressures.

Figure 6 presents the results obtained by varying the engine compression ratio in combination with the intake pressure, while maintaining a constant pressure difference Δp between intake and exhaust. Hydrogen is used as the fuel, and two combustion modes are considered, namely a stoichiometric mixture and a lean mixture ($\lambda = 2$).

Figure 6a,b show that both indicated and net electric efficiencies slightly increase with increasing compression ratio. However, some intersections are observed due to differences in the load coefficient that could be sustained under specific operating conditions, as shown in Figure 6e. Consistently with the results in Figure 5, increasing the intake pressure leads to a reduction in net electric efficiency due to the higher power demand of the compressor.

The indicated efficiency, on the other hand, is almost independent of intake pressure in the lean combustion case, whereas a more noticeable reduction is observed under stoichiometric conditions. This behavior is likely associated with the onset of engine instability as the maximum GLC is approached, leading to an advanced ignition position (Figure 6f) and a less favorable shape of the indicated cycle.

It is also worth noting that the indicated efficiency increases by approximately 10 percentage points when moving from stoichiometric to lean mixtures. Conversely, the effect of λ on net electric efficiency is mitigated by the contribution of compressor power, whose relative impact differs significantly between the two cases. Further analysis of the remaining plots shows that the power absorbed by the compressor increases with boost pressure, while remaining largely independent of compression ratio (Figure 6c).

Regarding net electric power (Figure 6d), increasing the compression ratio leads to a corresponding increase in power output. This effect is more pronounced under stoichiometric conditions, due to the higher chemical energy content of the mixture.

Overall, the results in Figure 6 indicate that the main engine performance parameters are primarily influenced by λ when GLC is set to its maximum value. Consistently with the results presented in Section 4, the effective compression ratio has a limited impact on the results, allowing its optimization based on fuel characteristics and performance targets.

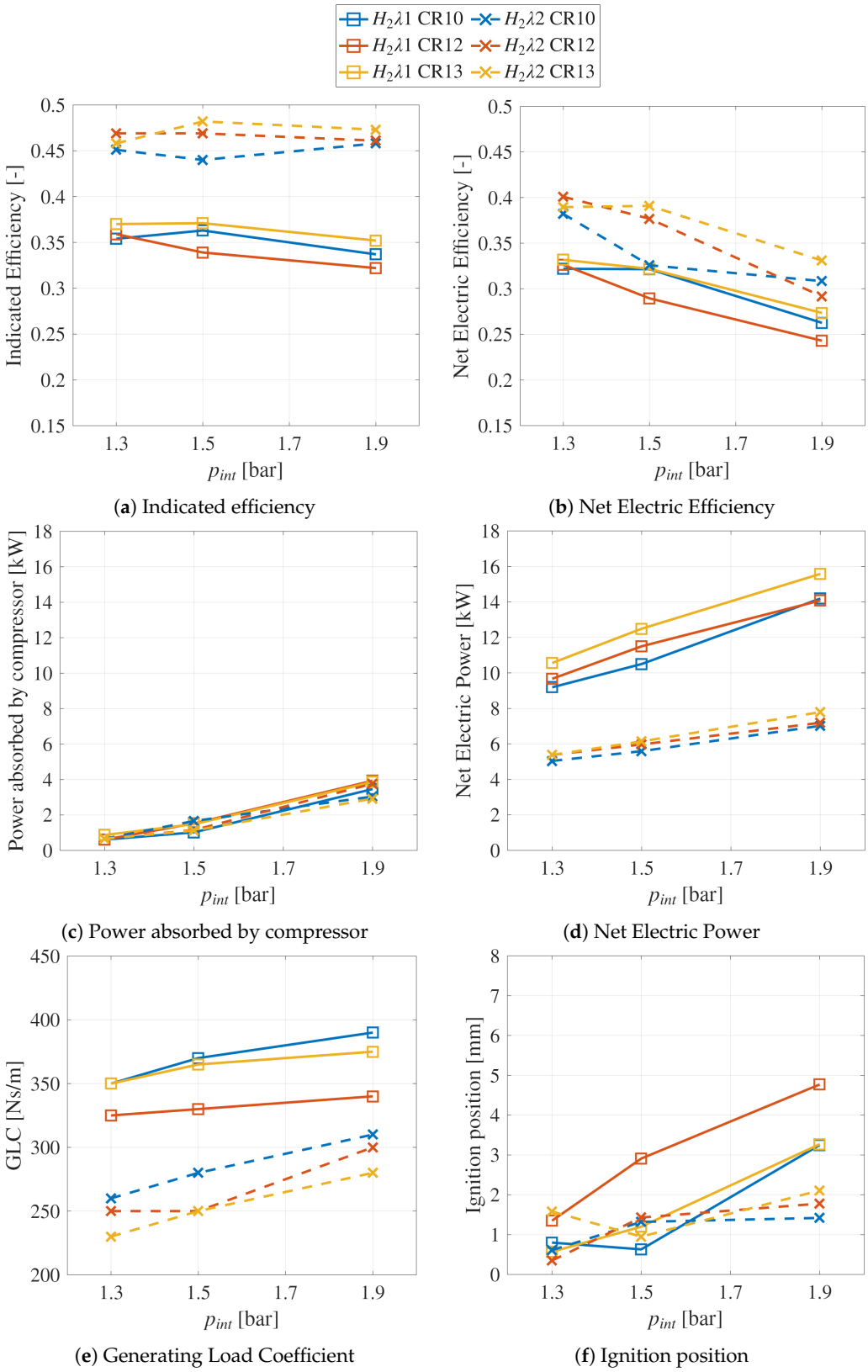

(**a**) Indicated efficiency (**b**) Net Electric Efficiency

(**c**) Power absorbed by compressor (**d**) Net Electric Power

(**e**) Generating Load Coefficient (**f**) Ignition position

Figure 6. Effect of variation in CR and intake pressure on the performance of the hydrogen-fueled engine at the maximum achievable GLC. Simulations are performed at constant intake–exhaust pressure difference Δp for two mixture conditions: stoichiometric and lean ($\lambda = 2$). Line and marker styles distinguish the two λ conditions as indicated in the legend, while colors identify the CR. Plots report: (**a**) indicated efficiency, (**b**) net electric efficiency, (**c**) compressor absorbed power, (**d**) net electric power, (**e**) generating load coefficient, and (**f**) ignition position relative to the nominal top dead center.

5.3. Engine Behavior with Different Fuels and Combustion Strategies

One of the main features of the FPLG is its capability to operate with different fuels without requiring modifications to the system architecture. This fuel flexibility has been widely highlighted in the literature as one of the key advantages of free-piston engines compared with conventional crankshaft engines [27]. In the following, engine performance at CR = 12 is analyzed by considering different fuel compositions (namely natural gas, hydrogen, and ethanol) and λ values (for hydrogen, $\lambda = 1$ and $\lambda = 2$ are considered). As in the previous subsection, the generating load coefficient is set to its maximum achievable value for each operating condition. Several operating points are investigated at different intake pressures, while maintaining a constant pressure difference Δp between intake and exhaust manifolds.

A preliminary observation is required before discussing this comparison in detail. Figure 7e shows that the maximum achievable load varies with intake pressure and, more significantly, with the selected fuel. This behavior is consistent with previous findings, particularly when comparing stoichiometric and lean hydrogen combustion: in the former case, the achievable electrical load is significantly higher.

A slight reduction in the maximum GLC at high intake pressure is observed for ethanol and may be associated with a more pronounced decrease in scavenging efficiency compared to hydrogen and natural gas (Figure 7f). This effect can lead to a higher fraction of residual gases in the combustion chamber, thereby reducing the effective energy content of the fresh charge. As a result, piston velocities and the work delivered by the piston decrease, requiring a reduction in the generating load coefficient to ensure stable operation. The resulting decrease in available energy also contributes to the efficiency loss observed for ethanol at high intake pressures (Figure 7a). A similar deviation from the general trend is observed in net electric power (Figure 7d), where ethanol shows a slower increase with intake pressure compared to the other fuels.

Considering only stoichiometric conditions, ethanol and natural gas exhibit comparable performance. Efficiency values (both indicated and net electric) are slightly higher for ethanol at low intake pressures and for natural gas at higher intake pressures (Figure 7a,b). A similar trend is observed for net electric power, which also reflects the reduction in ethanol GLC at higher intake pressures.

Notably, lean hydrogen loses its efficiency advantage at high intake pressures. This effect is further amplified by the lower maximum achievable GLC, resulting in lean hydrogen becoming less efficient than both natural gas and ethanol at an intake pressure of 1.9 bar, as shown in Figure 7b.

In summary, stoichiometric hydrogen combustion may be affected by abnormal combustion, high combustion temperatures, and increased NO_x emissions, and may therefore require dedicated strategies, such as EGR, to be effectively employed. This would lead to a reduction in the net power delivered by the generator. In contrast, stoichiometric natural gas and ethanol provide comparable performance in terms of both power and efficiency, with approximately 12 kW delivered at $p_{int} = 1.9$ bar. The indicated efficiency is around 0.40 in both cases, while the net electric efficiency is approximately 0.33 at the highest intake pressure considered.

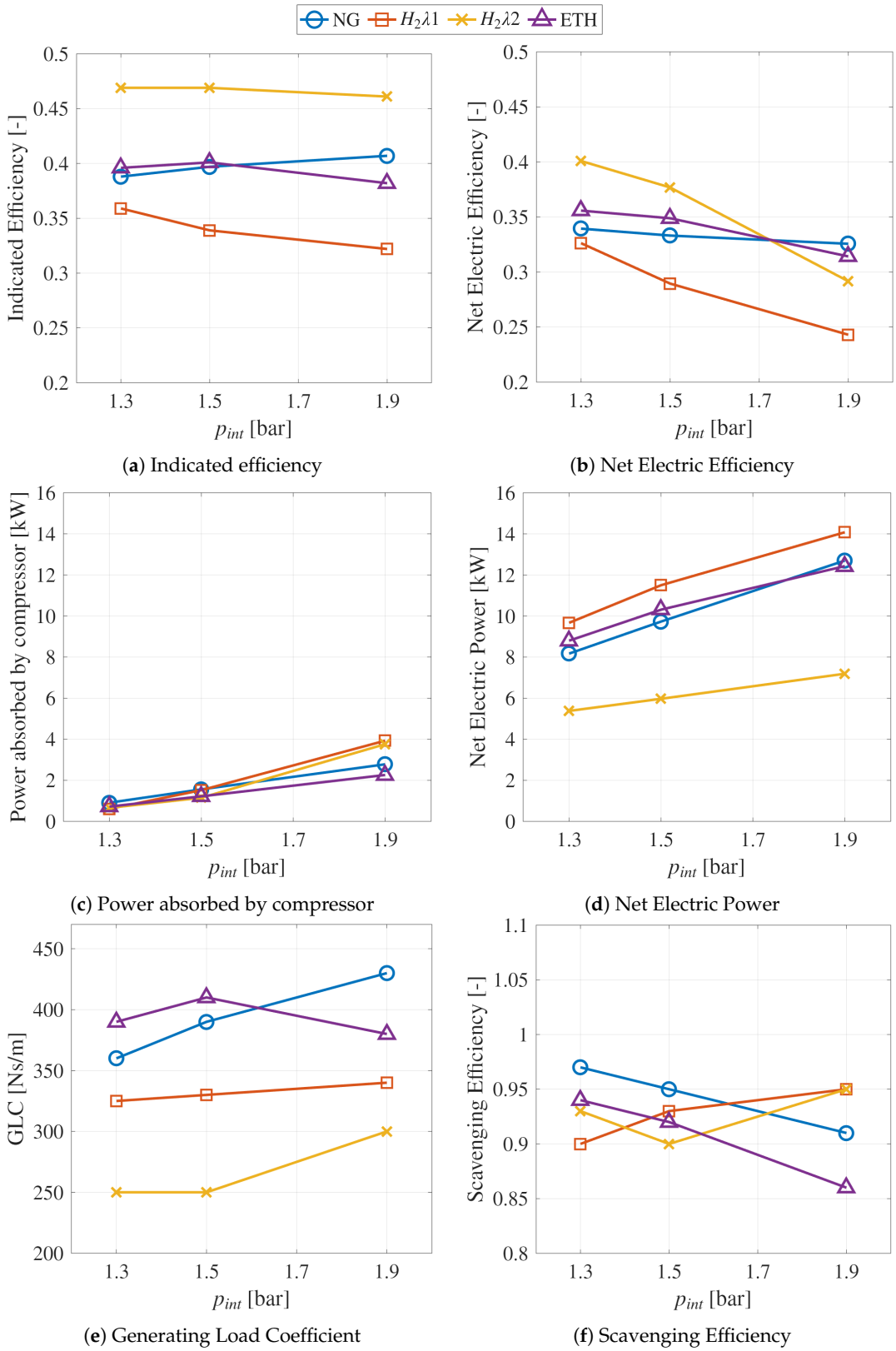

(**a**) Indicated efficiency (**b**) Net Electric Efficiency

(**c**) Power absorbed by compressor (**d**) Net Electric Power

(**e**) Generating Load Coefficient (**f**) Scavenging Efficiency

Figure 7. Comparison of engine performance for different fuels at a compression ratio of 12 and maximum achievable GLC. Simulations are performed at several intake pressures while maintaining a constant intake–exhaust pressure difference Δp. The fuels considered are natural gas, ethanol, hydrogen under stoichiometric conditions, and hydrogen under lean conditions. Colors and marker styles identify the different fuels as indicated in the legend. Plots report: (**a**) indicated efficiency, (**b**) net electric efficiency, (**c**) compressor absorbed power, (**d**) net electric power, (**e**) generating load coefficient, and (**f**) scavenging efficiency.

To contextualize the results obtained for the FPLG system, a comparison with published data on conventional range-extender ICE architectures was carried out. Table 10 summarizes the efficiency values reported in the literature for range-extender engines fueled with different fuels, alongside the corresponding results obtained in the present work. It should be noted that a direct comparison is hindered by the limited availability of studies featuring similar engine configurations and operating conditions, as well as by the use of different efficiency metrics across the referenced works. For this reason, the most relevant efficiency parameter reported in each reference is presented, while both indicated efficiency and net electric efficiency are reported for the present work, so as to provide the broadest possible basis for comparison.

Table 10. Benchmarking of net electric/brake efficiency against conventional range-extender ICE architectures.

Source	Engine Type/Fuel	Efficiency Metric	Value
[28]	2-stroke, gasoline	Gross indicated/brak	0.37–0.43/0.32–0.38
[29]	4-stroke, ethanol, CR 12	Brake efficiency	0.34–0.38
[30]	4-stroke, LPG	Peak brake efficiency	0.274
[31]	4-stroke, H_2, $\lambda = 2$	Range-extender efficiency	∼0.20
Present work	FPLG, NG/ethanol, $\lambda = 1$, CR 12	Net electric efficiency	0.33–0.36
	FPLG, H_2, $\lambda = 2$, CR 12	Net electric efficiency	0.29–0.40
	FPLG, NG/ethanol, $\lambda = 1$, CR 12	Indicated efficiency	0.38–0.40
	FPLG, H_2, $\lambda = 2$, CR 12	Indicated efficiency	0.46–0.47

The results obtained for the FPLG system under stoichiometric natural gas and ethanol operation are broadly consistent with those reported for conventional range-extender architectures. The indicated efficiency of 0.38–0.40 compares favorably with the gross indicated efficiency of 0.37–0.43 reported for an optimized two-stroke gasoline range-extender engine [28] and with the brake efficiency of 0.34–0.38 obtained for an ethanol-fueled four-stroke engine at a comparable compression ratio [29]. The net electric efficiency of 0.33–0.36, which accounts for the power consumed by the electrically driven supercharger, is in line with the brake efficiency figures reported for conventional architectures [28,29], and substantially exceeds the peak brake efficiency of 0.274 reported for the LPG-fueled range-extender engine [30]. Regarding hydrogen operation, the net electric efficiency of 0.29–0.40 achieved under lean combustion ($\lambda = 2$) in the present work spans a wider range, reflecting the strong sensitivity of performance to intake pressure already discussed in Section 4. This compares favorably with the total range-extender efficiency of approximately 0.20 reported in [31] for a converted gasoline engine operating at $\lambda = 2$. The discrepancy can be attributed to the additional mechanical and electrical losses inherent in a converted conventional architecture, as well as to the different definition of efficiency adopted in that reference. It should, however, be noted that the results presented here are based on numerical simulations, and experimental validation remains a necessary step before definitive conclusions can be drawn. Overall, the benchmarking exercise confirms that the opposed-piston FPLG concept is competitive with, and in several cases superior to, conventional range-extender architectures in terms of both thermal and net electric efficiency, while offering the additional advantages of fuel flexibility and variable compression ratio operation without any mechanical reconfiguration.

6. Conclusions

The present work investigated the parameters governing the performance and efficiency of spark-ignition opposed-piston free-piston linear generators through a numerical approach. Simulations were performed using a one-dimensional model suitably extended to account for the effects of electrical load and gas spring pressure on piston dynamics.

A Design of Experiments methodology based on a Sobol sequence was adopted to systematically explore the influence of design and operating parameters. This approach enabled the identification of cause–effect relationships between input variables and engine performance indicators.

The resulting dataset was further analyzed through a correlation analysis to quantify the combined influence of the input parameters on the system response. This analysis also allowed the identification of synergistic and compensating effects between variables. The derived regression models provide a useful tool for the preliminary screening of unfavorable parameter combinations, allowing unsuitable design or operating conditions to be excluded at an early stage of the development process.

The potential of hydrogen as a fuel for FPLG applications was also assessed by considering both stoichiometric and lean operating conditions. The effects of generating load coefficient, boost pressure, and compression ratio were analyzed in order to evaluate their impact on performance and efficiency. Furthermore, the capability of the FPLG to operate with a variable compression ratio enabled a direct comparison between different fuels, namely natural gas, hydrogen, and ethanol.

The main findings of this study can be summarized as follows:

- The correlation analysis of the DoE simulations highlighted the dominant influence of the generating load coefficient on IMEP, indicated efficiency, BSFC, and net electric power.
- When the generating load coefficient is set to its maximum achievable value, the main performance parameters are primarily affected by the air–fuel equivalence ratio λ. The effective compression ratio plays a secondary role, suggesting that it can be selected based on fuel properties and combustion constraints rather than being a primary optimization variable.
- Stoichiometric hydrogen combustion may be affected by abnormal combustion phenomena, high combustion temperatures, and increased NO_x emissions, and may therefore require dedicated strategies such as exhaust gas recirculation. This implies a potential penalty in terms of net power output, which should be carefully considered when evaluating hydrogen-based operation.
- Stoichiometric natural gas and ethanol provide comparable performance in terms of both power and efficiency, confirming the strong fuel-flexibility potential of the free-piston engine concept. Approximately 12 kW can be delivered at $p_{int} = 1.9$ bar, with indicated efficiency values around 0.40 and net electric efficiency values around 0.33.
- Overall, the FPLG concept emerges as a competitive solution for range-extender applications, capable of achieving performance levels comparable to conventional architectures while offering additional flexibility in fuel selection and operating conditions. Further research is required to improve control strategies and to enhance system efficiency through advanced exhaust energy recovery solutions.

Author Contributions: Conceptualization, M.B.; Methodology, M.B. and D.A.M.; software, A.S. and F.S.; validation, A.S. and F.S.; formal analysis, all; investigation, A.S. and F.S.; writing—original draft preparation, A.S., F.S. and M.B.; writing—review and editing, M.B. and D.A.M.; supervision, M.B. and D.A.M.; project administration, M.B.; funding acquisition, M.B. All authors have read and agreed to the published version of the manuscript.

Funding: The authors acknowledge financial support under the National Recovery and Resilience Plan (NRRP), Mission 4, Component 2, Investment 1.1, Call for tender No. 104 published on 2 February 2022 by the Italian Ministry of University and Research (MUR), funded by the European Union–NextGenerationEU–Project Title FLEX-GEN–CUP B53D23005670006—Grant Assignment Decree No. 961 adopted on 30 June 2023 by the Italian Ministry of Ministry of University and Research (MUR).

Data Availability Statement: Data are not available due to confidentiality constraints.

Acknowledgments: The valuable contribution of Tommaso Lucchini, Politecnico di Milano, and Carlo Beatrice, Science and Technology for Sustainable Mobility (STEMS), is aknowledged within the Flex-Gen research project.

Conflicts of Interest: The authors declare no conflict of interest.

Abbreviations

The following abbreviations are used in this manuscript:

1D	One-Dimensional
3D	Three-Dimensional
AFR	Air–Fuel Ratio
BDC	Bottom Dead center
BSFC	Brake Specific Fuel Consumption
CFD	Computational Fluid Dynamics
CO	Carbon Monoxide
CO_2	Carbon Dioxide
CR	Compression Ratio
DoE	Design of Experiments
FPLG	Free-Piston Linear Generator
GHG	Greenhouse Gas
GLC	Generating Load Coefficient
H_2	Hydrogen
HC	Hydrocarbons
HCCI	Homogeneous Charge Compression Ignition
HRR	Heat Release Rate
ICE	Internal Combustion Engine
IMEP	Indicated Mean Effective Pressure
LPG	Liquefied Petroleum Gas
NG	Natural Gas
NMHC	Non-Methane Hydrocarbons
NO_x	Nitrogen Oxides
PCC	Pearson's Correlation Coefficient
PCCI	Premixed Charge Compression Ignition
PI	Proportional-Integral
R^2	Coefficient of Determination
RMSE	Root mean Square Error
TDC	Top Dead center
THC	Total Hydrocarbons

References

1. Misul, D.; Baratta, M.; Xu, J.; Fuerhapter, A.; Heindl, R. Experimental and CFD Investigation of Fuel Mixing in an Optical-Access Direct-Injection NG Engine and Correlation with Test Rig Combustion and Performance Data. *Energies* **2023**, *16*, 3004. [CrossRef]
2. Maggio, G.; Nicita, A.; Squadrito, G. How the hydrogen production from RES could change energy and fuel markets: A review of recent literature. *Int. J. Hydrogen Energy* **2019**, *44*, 11371–11384. [CrossRef]

3. Verhelst, S.; Wallner, T. Hydrogen-fueled internal combustion engines. *Prog. Energy Combust. Sci.* **2009**, *35*, 490–527. [CrossRef]
4. Bielaczyc, P.; Woodburn, J.; Gandyk, M.; Szczotka, A. Ethanol as an automotive fuel—A review. *Combust. Engines* **2016**, *166*, 39–45. [CrossRef]
5. Liu, L.; Zhang, M.; Liu, Z. A Review of Development of Natural Gas Engines. *Int. J. Automot. Manuf. Mater.* **2023**, *2*, 4. [CrossRef]
6. Mikalsen, R.; Roskilly, A. A review of free-piston engine history and applications. *Appl. Therm. Eng.* **2007**, *27*, 2339–2352. [CrossRef]
7. Hanipah, M.R.; Mikalsen, R.; Roskilly, A. Recent commercial free-piston engine developments for automotive applications. *Appl. Therm. Eng.* **2015**, *75*, 493–503. [CrossRef]
8. Hung, N.B.; Lim, O. A review of free-piston linear engines. *Appl. Energy* **2016**, *178*, 78–97. [CrossRef]
9. Guo, C.; Zuo, Z.; Feng, H.; Jia, B.; Roskilly, T. Review of recent advances of free-piston internal combustion engine linear generator. *Appl. Energy* **2020**, *269*, 115084. [CrossRef]
10. Raheem, A.T.; A. Aziz, A.R.; A. Zulkifli, S.; Rahem, A.T.; Ayandotun, W.B. A review of free piston engine control literature—Taxonomy and techniques. *Alex. Eng. J.* **2022**, *61*, 7877–7916. [CrossRef]
11. Brosnan, P.; Tian, G.; Montanaro, U.; Cockerill, S. A Comprehensive Review of the Free Piston Engine Generator and Its Control. *Int. J. Automot. Manuf. Mater.* **2023**, *2*, 27. [CrossRef]
12. Guo, C.; Feng, H.; Jia, B.; Zuo, Z.; Guo, Y.; Roskilly, T. Research on the operation characteristics of a free-piston linear generator: Numerical model and experimental results. *Energy Convers. Manag.* **2017**, *131*, 32–43. [CrossRef]
13. Huang, F.; Kong, W. Effects of hydrogen addition on combustion characteristics of a free-piston linear engine with glow-assisted ignition. *Int. J. Hydrogen Energy* **2021**, *46*, 23040–23052. [CrossRef]
14. Schneider, S.; Chiodi, M.; Friedrich, H.; Bargende, M. Development and Experimental Investigation of a Two-Stroke Opposed-Piston Free-Piston Engine. In Proceedings of the SAE/JSAE 2016 Small Engine Technology Conference & Exhibition, Charleston, SC, USA, 15–17 November 2016; No. 2016-32-0046. [CrossRef]
15. Zhang, Q.; Xu, Z.; Liu, S.; Liu, L. Effects of Injector Spray Angle on Performance of an Opposed-Piston Free-Piston Engine. *Energies* **2020**, *13*, 3735. [CrossRef]
16. Liu, S.; Xu, Z.; Chen, L.; Liu, L. Comparison of an opposed-piston free-piston engine using single and dual channel uniflow scavenging. *Appl. Therm. Eng.* **2022**, *201*, 117813. [CrossRef]
17. Morandi, N.; Lucchini, T.; Gianetti, G.; Baratta, M.; Misul, D.; Santonocito, F. Parametric Analysis of Performance and Efficiency of Free-Piston Linear Generators with 1D and CFD Simulations. In Proceedings of the 17th International Conference on Engines and Vehicles, Capri, Italy, 14–17 September 2025; No. 2025-24-0105. [CrossRef]
18. Heywood, J. *Internal Combustion Engine Fundamentals*, 2nd ed.; McGraw-Hill Education: New York, NY, USA, 2019.
19. Borman, G.; Nishiwaki, K. Internal-combustion engine heat transfer. *Prog. Energy Combust. Sci.* **1987**, *13*, 1–46. [CrossRef]
20. Jia, B.; Zuo, Z.; Tian, G.; Feng, H.; Roskilly, A. Development and validation of a free-piston engine generator numerical model. *Energy Convers. Manag.* **2015**, *91*, 333–341. [CrossRef]
21. Sobol', I. On the distribution of points in a cube and the approximate evaluation of integrals. *USSR Comput. Math. Math. Phys.* **1967**, *7*, 86–112. [CrossRef]
22. Sun, X.; Roberts, S.; Croke, B.; Jakeman, A. A comparison of global sensitivity techniques and sampling method. In Proceedings of the 22nd International Congress on Modelling and Simulation, MODSIM 2017, Hobart, Australia, 3–8 December 2017. [CrossRef]
23. Della Torre, A.; Montenegro, G.; Cerri, T.; Onorati, A. A 1D/Quasi-3D Coupled Model for the Simulation of I.C. Engines: Development and Application of an Automatic Cell-Network Generator. *SAE Int. J. Engines* **2017**, *10*, 471–482. [CrossRef]
24. Baratta, M.; Di Mascio, V.; Misul, D.; Marinoni, A.; Cerri, T.; Onorati, A. *Development of a NG Engine Predictive Simulation Model and Investigation of Engine Performances Under Hydrogen-Blended Operation*; In Proceedings of SAE Technical Conference on Sustainable Mobility, Catania, 18–20 September 2024; No. 2024-24-0029. [CrossRef]
25. Pearson, K. VII. Mathematical contributions to the theory of evolution.—III. Regression, heredity, and panmixia. *Philos. Trans. A Math. Phys. Eng. Sci.* **1896**, *187*, 253–318. [CrossRef]
26. Yang, F.; Feng, H.; Wu, L.; Zhang, Z.; Wang, J. Performance prediction and parameters optimization of an opposed-piston free piston engine generator using response surface methodology. *Energy Convers. Manag.* **2023**, *295*, 117633. [CrossRef]
27. Zhang, Z.; Feng, H.; Zuo, Z. Numerical Investigation of a Free-Piston Hydrogen-Gasoline Engine Linear Generator. *Energies* **2020**, *13*, 4685. [CrossRef]
28. Borghi, M.; Mattarelli, E.; Muscoloni, J.; Rinaldini, C.A.; Savioli, T.; Zardin, B. Design and experimental development of a compact and efficient range extender engine. *Appl. Energy* **2017**, *202*, 507–526. [CrossRef]
29. Martinez, S.; Weissinger, F.; Lacava, P.T.; Mendoza, A.P.; Martelli, A.; Rufino, C.H.; Curto-Risso, P. Enhancing Efficiency of Ethanol-Powered Range Extenders in the Bmw I3: A Simulation-Based Optimization Approach. *Renew. Energy* **2025**, *251*, 123394. [CrossRef]

30. Lasocki, J.; Kopczyński, A.; Krawczyk, P.; Roszczyk, P. Empirical Study on the Efficiency of an LPG-Supplied Range Extender for Electric Vehicles. *Energies* **2019**, *12*, 3528. [CrossRef]
31. Noga, M.; Moskal, T. Conversion to hydrogen fueling of a range extender SI engine of a 48 V hybrid electric vehicle. *Combust. Engines* **2026**, *204*, 66–71. [CrossRef]

Disclaimer/Publisher's Note: The statements, opinions and data contained in all publications are solely those of the individual author(s) and contributor(s) and not of MDPI and/or the editor(s). MDPI and/or the editor(s) disclaim responsibility for any injury to people or property resulting from any ideas, methods, instructions or products referred to in the content.